RESEARCH ACTIVITIES VI
Department of Vacuum UV Photoscience

VI-A Electronic Structure and Decay Mechanism of Inner-Shell Excited Molecules

This project is being carried out at the Beamline 4B of the UVSOR facility. We have three subprojects: (A) spin-orbit, exchange, and molecular field splittings in S 2*p* and P 2*p* excited states, (B) molecules and radicals in condensed phase and in rare gas matrix, and (C) ionic fragmentations following the inner-shell resonance excitation. In (A), we have found some spin-forbidden ionized and excited states in non-radiative (photoelectron emission) and radiative (photon emission) deexcitation spectra in collaboration with the Uppsala University. In (C), we are concentrating on theoretical interpretation of our experimental data measured for last several years.

VI-A-1 Spin-Forbidden Shake-Up States in the Valence Ionization of CS_2

HATSUI, Takaki; NAGASONO, Mitsuru[1]; SHIGEMASA, Eiji; KOSUGI, Nobuhiro
([1]Kyoto Univ.)

Photoelectron spectroscopy (PES) is widely used to investigate the one-electron energy level in various systems. All lines which have been observed so far in PES are doublet ionized state in the case of molecules with singlet ground state. The shake-up satellites can be enhanced by exciting at resonances. In this report we for the first time demonstrate that invisible (dark) spin-forbidden states in non-resonant PES can be observed by PES at sulfur 2*p* resonances with strong singlet-triplet mixing *via* spin-orbit coupling of the sulfur 2*p* core electrons. Figure 1 shows an example of our PES of CS_2, recorded on the S $2p_{3/2} \rightarrow 3\pi_u^*$ resonance and below the resonance. Within the (LS) coupling scheme, the excited states are described as strongly mixed states with singlet and triplet components, where the intensity comes from dipole-allowed singlet components. Intermediate states in the resonant PES have triplet components as well, which open up transitions to quartet ionized states in addition to doublet states. Satellite 0 is not observed in the non-resonant spectrum at all. Satellite 1 is assigned to the lowest doublet shake-up state with the $^2\Pi_u$ symmetry [1] allowed in the non-resonant PES spectra. The satellite 0 is assigned to a transition to the quartet counterpart ($^4\Pi_u$) of the doublet state based on ab initio configuration interaction calculations.

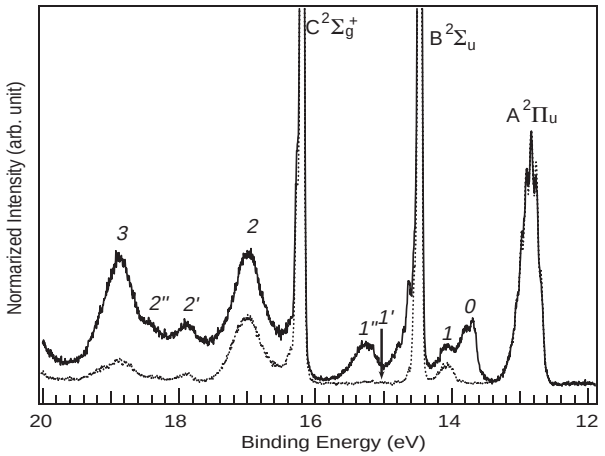

Figure 1. PES spectrum of CS_2 recorded at the $2p_{3/2} \rightarrow 3\pi_u^*$ resonance (163.22 eV) and non-resonant spectrum recorded below the sulfur 2*p* excitation region (151.2 eV).

Reference

1) P. Baltzer *et al.*, *Chem. Phys.* **202**, 185 (1996).

VI-A-2 Spin- and Symmetry Forbidden Ionized States of OCS Molecule

MASUDA, Suomi[1]; HATSUI, Takaki; SHIGEMASA, Eiji; KOSUGI, Nobuhiro
([1]GUAS)

Some satellite structures in the photoelectron spectrum (PES) are enhanced by exciting at the resonances. In this work, we have measured resonant PESs of OCS molecule and successfully found the spin- and symmetry forbidden shake-up states ($^4\Pi$ and $^2\Phi$) as well as the lowest double shake-up state ($^2\Pi$).

Photoabsorption spectrum of OCS shows transitions to $4\pi^*$, $10\sigma^*$ and Rydberg states below the sulfur 2*p* ionization threshold. Due to the spin-orbit interaction, each transition is split into the $2p_{3/2}$ and $2p_{1/2}$ manifolds. Figure 1 shows resonant PES of OCS at the $2p_{3/2} \rightarrow 4\pi^*$ resonance (solid line) as well as an off-resonance one (dotted line). In the non-resonant PES, a very week band 1 is clearly observed, which is assigned to the lowest $^2\Pi$ shake-up satellite, of which the intensity is borrowed from the A state ($^2\Pi(2\pi^{-1})$). In the resonant case, additional strong satellite bands 0 and 2 are found. These satellites are not observed in the non-resonant PES. Based on ab initio MRCI calculations, the bands 0

and 1 are assigned to the quartet and doublet Π satellites with the ($3\pi_x^{-1}$ $3\pi_y^{-1}$ $4\pi^{+1}$) electron configuration. The Band 2 is assigned to be the lowest symmetry-forbidden $^2\Phi$ states.

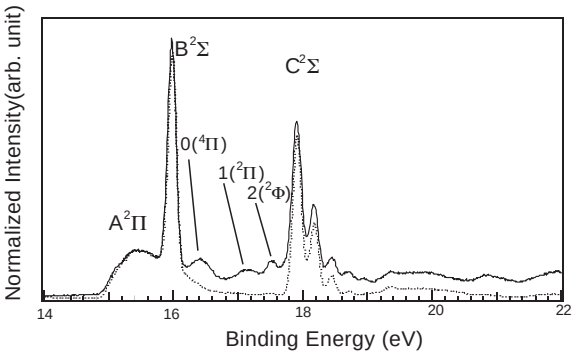

Figure 1. Photoelectron spectra of OCS molecule excited at the $2p_{3/2} \rightarrow 4\pi^*$ resonance (164.4 eV) (solid line) and at off-resonance 10 eV below the $2p_{3/2} \rightarrow 4\pi^*$ resonance (doted line).

VI-A-3 Measurements of Sulfur 2*p* Photoelectron and Sulfur L-emission of SF_6 at Sulfur 2*p* Resonances

KOSUGI, Nobuhiro; HATSUI, Takaki; GUO, Jinghua[1]; NORDGREN, Joseph[2]
([1]Lawrence Livermore Natl. Lab.; [2]Uppsala Univ.)

The sulfur 2*p* photoabsorption spectrum of SF_6 molecule shows strong valence excitations and shape resonances as well as very week Rydberg series (inset in Figure 1), which are characteristic of systems surrounded by electronegative atoms. In this study, sulfur 2*p* photoelectron spectra and sulfur *L*-emission spectra have been measured at these resonances. At the resonances below the threshold, triplet valence excited states are found in the soft x-ray emission spectra through singlet-triplet mixed 2*p* exciteations due to the spin-orbit interaction. Above the ionization threshold, dependence upon the excitation energy is generally small in most cases because non-resonant contribution is dominant. In the case of SF_6, the branching ratio between $2p_{3/2}$ and $2p_{1/2}$ photoelectron peaks, however, shows distinct variation upon the excitation energy in photoelectron spectra (Figure 1) and emission spectra. These behaviour has been atttributed to the strong exchange interaction between core hole and excited electron at the resonances.

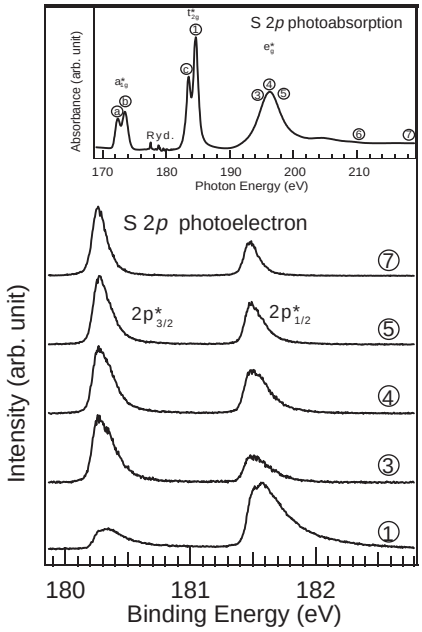

Figure 1. Photoelectron spectra of SF_6 recorded at the sulfur 2*p* resonances (shown in inset).

VI-A-4 N 1*s* Photoabsorption of N_2 Trapped in Rare Gas Matrices

NAGASONO, Mitsuru[1]; OJI, Hiroshi; HATSUI, Takaki; SHIGEMASA, Eiji; KOSUGI, Nobuhiro
([1]Kyoto Univ.)

The gaseous N_2 spectrum shows complex structures in the N 1*s* threshold region, resulting from resonances by transitions into π*, σ*, Rydberg and multiple-electron excited states. Some of them have diffuse character and should have environmental effects around the molecule. In the present work, we have measured N 1*s* excitation spectra of N_2 trapped in rare gas matrices.

On a new beamline BL4B at UVSOR, N 1*s* photoabsorption spectra were measured with an electron yield method for rare-gas matrix isolated and condensed N_2, and with a transmission method for gaseous N_2. Samples were prepared by mixing gaseous N_2 with rare gas, Ne, Ar, Kr or Xe, in a vacuum vessel and evaporated on an Au coated Cu plate. The temperature of the plate was below 6.5 K by a cryostat. The ratios N_2 to rare gas were 1/10 and 1/1.

Figure 1 shows that 3*s* and 3*p* Rydberg-like excited states exhibit blue shifts in photon energy in the matrix phase. The shift of the Rydberg excitation energy is determined by competition between the shifts of the ionization potential and the term value. The ionization potential becomes smaller as the distance between the N_2 and the neighbors, or the cage size, smaller. On the other hand, the term value is related to the antibonding character in the Rydberg state, and the antibonding character depends on the overlap of the Rydberg orbital with the valence orbital of the neighbor species; that is, the term value becomes smaller as the cage size smaller. Thus, the observed matrix effect indicates that the variation of the term value for the 3*s* and 3*p* Rydberg is larger than that of the ionization potential.

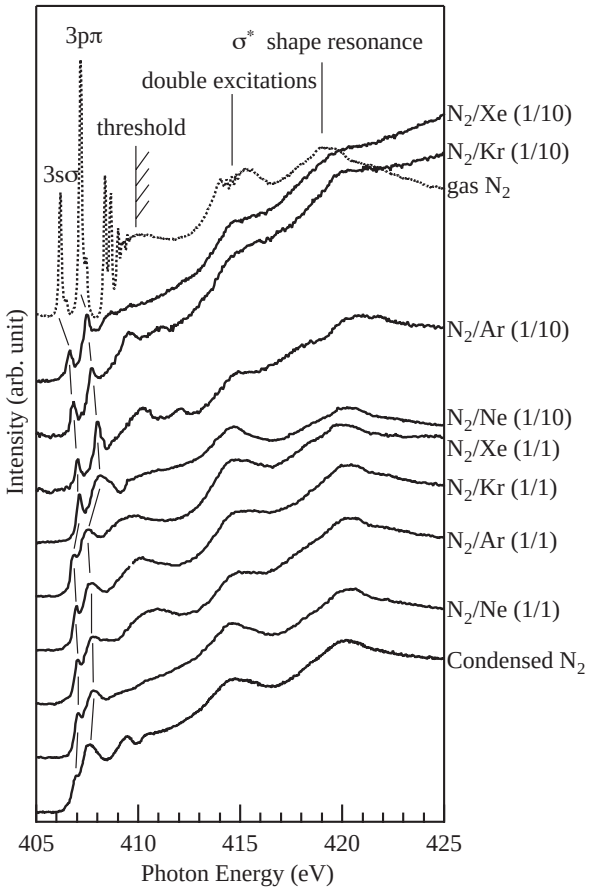

Figure 1. The N 1*s* photoabsorption spectra near the N 1*s* ionization threshold region for the N_2 in gaseous phase, rare gas matrix phases and condensed phase.

VI-A-5 Ab Initio CI Calculation for O1*s* → σ* Core-Excited States of Ozone: Difference in Direction between Transition Dipole Moment and Photodissociation

OJI, Hiroshi; KOSUGI, Nobuhiro

The transition dipole moment ($\boldsymbol{\mu}$) for the O1*s* → σ*($7a_1$) excitation of O_3 were calculated by *ab initio* configuration interaction (CI) method. Accurate evaluation of $\boldsymbol{\mu}$ is necessary to investigate detailed dynamics of photodissociation of polyatomic molecules following the core-excitation, since the direction of $\boldsymbol{\mu}$ with respect to the bond axis acts as an essential factor in determining the anisotropy parameter for fragment species. We have examined molecular structure dependence of $\boldsymbol{\mu}$ by changing the length of one bond in O_3.

The molecular structure of O_3 with the definitions of bond-length R, R', ϕ and the axes of coordinates are illustrated in Figure 1(a). The MO patterns for ground and core-excited states at the equilibrium structure (R = R' = 0.127 nm, ϕ = 118˚) obtained by one electron approximation are shown in Figure 1(b). In the ground state, the shape of MO reflects its C_{2v} symmetry and there is some deviation between the direction of $\boldsymbol{\mu}$ and that of O_a–O_c bond axis. In the core excited state, the shape is strongly distorted by core excitonic effect, but $\boldsymbol{\mu}$ is not still parallel with the bond. The results of CI calculation was θ = 8.34˚, as seen in Table 1. If the length of R is shortened, θ becomes larger. On the other hand, when R is lengthened, θ gradually decreases, but does not become almost 0 until R = 0.25 nm. The present results indicate that the direction of the 1*s* → σ* transition dipole $\boldsymbol{\mu}$ is not always parallel to the σ bond and more or less affected by the neighboring atoms that are not directly connected with the core-excited atom.

Table 1. Results of the CI calculation for the components of $\boldsymbol{\mu}$ (μ_x, μ_z) and the angle between the directions of $\boldsymbol{\mu}$ and O_a–O_c bond (θ) as functions of R, when the terminal O (O_a) core is excited.

R / nm	μ_x / a.u.	μ_z / a.u.	θ / deg
0.120	0.013663	–0.038903	19.35
0.125	0.019042	–0.050656	12.19
0.127	**0.007505**	**–0.051173**	**8.34**
0.140	0.004682	–0.054426	4.92
0.170	0.003143	–0.054332	3.31
0.200	0.002290	–0.055824	2.35
0.250	0.000128	–0.057585	0.13

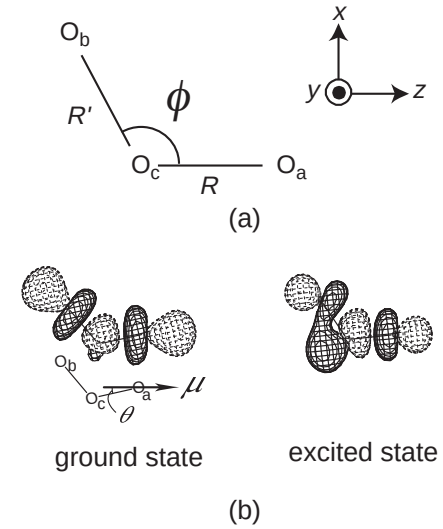

Figure 1. (a) The structure of O_3. The axis of coordinate used in the calculation is also illustrated. (b) MO patterns of σ*($7a_1$) of O_3 in the ground and excited states when the terminal oxygen (O_a) core is excited. The definition of the angle θ is illustrated.

VI-B Soft X-Ray Photoelectron-Photoabsorption Spectroscopy and Electronic Structure of Transition Metal Compounds

In this project, we were using the crystal monochromator Beamline 1A of the UVSOR facility, which restrict the photon energy to the range higher than the Ni 2*p* edge (> 800 eV), but now are using Beamline 4B, covering the lower photon energy (< 800 eV). We can excite the first row elements to their 1*s* resonance states. We are interested in linear polarization dependence of inner-shell resonant excitations for planar complex molecules/ions in the single crystal, and in resonantly-emitted photoelectron by tuning the photon energy to inner-shell resonances. Dr. Hiroshi Oji has been working as a postdoctoral IMS fellow since April 2000, and Dr. Takaki Hatsui as a research associate since August 2000.

VI-B-1 B 1*s*- and La 4*d*-Edge Photoabsorption and Resonant Photoelectron Spectroscopy of Rare-Earth Borocarbide LaB_2C_2

OJI, Hiroshi; HASEGAWA, Shinji; SUZUKI, Kazuya[1]; KOSUGI, Nobuhiro
([1]Yokohama Natl. Univ.)

Last year we reported the La 3*d*-edge X-ray absorption spectroscopic (XAS) and valence-band resonant photoelectron spectroscopic (RPES) studies of lanthanum borocarbide (LaB_2C_2) at UVSOR-BL1A, where we could obtain the information about the degree of charge transfer between La atoms and BC sheets. In the present work, B 1*s*-edge (~ 200 eV) and La 4*d*-edge (~ 100 eV) XAS and valence-band RPES were measured at the BL4B soft X-ray beamline of the UVSOR facility to obtain further information about the electronic structure of LaB_2C_2.

La 4*d*-edge XAS spectrum of LaB_2C_2 is shown in Figure 1. The assignments of the peaks are indicated in the figure.[1)] The valence- and inner-valence RPES spectra of LaB_2C_2 at various photon energies (indicated by numbers) are shown in Figure 2. Abscissa corresponds to the binding energy relative to the Fermi level (E_F). La 5*p* bands (~ 20 eV) are significantly enhanced in the on-resonant (La 4*d*) spectrum. Especially, an anomalous change of the photoemission branching ratio between $5p_{3/2}$ and $5p_{1/2}$ intensity can be seen. Actually, this anomaly is also observed in other La compounds. Ogasawara *et al*. attributed this to the multiplet dependence of the Auger transition probabilities.[1)] The intensity of the all valence- and inner-valence band begins to decrease from the photon energy of "5," and almost no structure can be observed at "10." Such a phenomenon was not observed in the RPES spectra at B *K*-edge (not shown here).

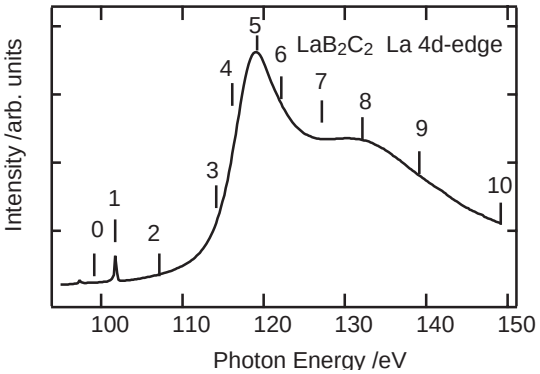

Figure 1. La 3*d*-edge XAS spectrum of LaB_2C_2.

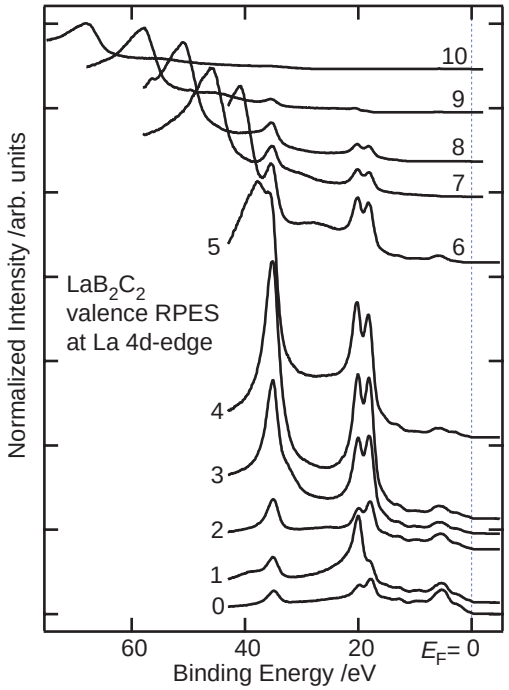

Figure 2. The valence and inner-valence RPES spectra of LaB_2C_2 of various photon energies.

Reference

1) H. Ogasawara *et al.*, *Solid State Commun.* **81**, 645 (1992).

VI-C Observation of Vibrational Coherence (Wavepacket Motion) in Solution-Phase Molecules Using Ultrashort Pulses

With recent remarkable improvements of ultrashort-pulse lasers, we are now able to generate an optical pulse shorter than a few tens of femtoseconds. Owing to its ultrashort duration and broad frequency bandwidth, the ultrashort pulse can excite a molecule 'impulsively' to generate a coherent superposition of vibrational eigen states either in the excited state or in the ground state. This vibrationally coherent state evolves in time, which is called wavepacket motion. The observation and control of the wavepacket motion is one of the most interesting topics in modern spectroscopy. In this project, we study vibrational coherence in the condensed-phase molecules by using ultrashort optical pulses having a duration of ten ~ a few tens of femtoseconds.

VI-C-1 Excited-State Vibrational Coherence of Solution-Phase Molecules Observed in the Third-Order Optical Process Using Extremely Short Pulses

TAKEUCHI, Satoshi; FUJIYOSHI, Satoru[1]; TAHARA, Tahei[2]
([1]GUAS; [2]IMS and RIKEN)

[*RIKEN REVIEW* in press]

Excited-state vibrational coherence of solution-phase polyatomic molecules was studied by two different time-domain spectroscopic methods. Raman-active low-frequency vibrations in the excited state of *trans*-stilbene were observed through transient impulsive stimulated Raman scattering spectroscopy. In transient absorption spectroscopy with a 40-fs resolution, a different vibrational mode of the same excited state was observed as a "beat" in the pump-induced absorption signal. We discussed the selection of the vibrational modes by noting the difference in the third-order optical processes relevant to the two spectroscopies. The vibrational coherence of a "reacting" excited state was also observed for ultrafast photodissociation of diphenylcyclopropenone.

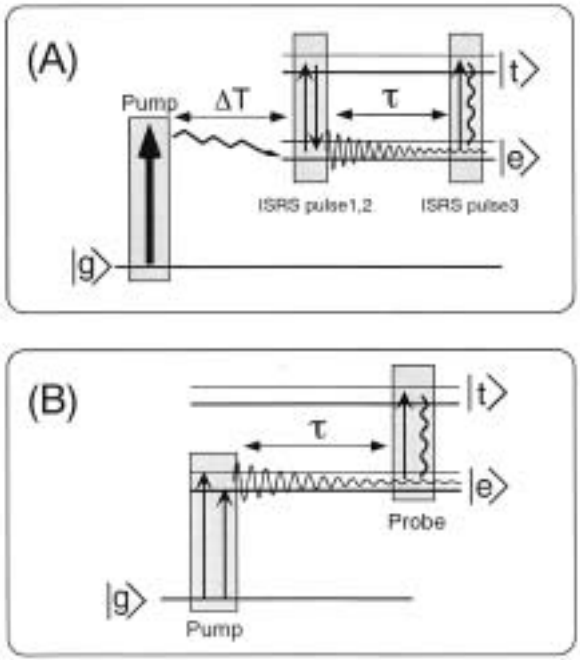

Figure 1. The third-order optical processes utilized to observe the excited-state vibrational coherence. (A) transient ISRS, (B) transient absorption.

VI-D Studies of Primary Photochemical/Physical Processes Using Femtosecond Electronic Spectroscopy

Ultrafast spectroscopy is playing an essential role in elucidation of photochemical reactions. Thanks to the recent advance in laser technology, we are now able to examine the dynamics of chemical reactions that take place in the femtosecond time region. In this project, we study primary photochemical/physical processes of the condensed-phase molecules using time-resolved fluorescence and absorption spectroscopy whose time-resolution is a few hundreds femtoseconds. Time-resolved fluorescence and absorption spectroscopy are complimentary to each other. The advantage of fluorescence spectroscopy lies in the fact that fluorescence originates from the transition between the "well-known" ground state and the excited state in question. Thus time-resolved fluorescence spectroscopy can afford unique information not only about the dynamics but also other properties of the excited singlet states such as their energies and oscillator strengths. On the other hand, however, time-resolved absorption spectroscopy is considered to be more versatile because it can detect not only fluorescent excited singlet states but also other "dark" transients.

VI-D-1 Femtosecond/Picosecond Time-Resolved Spectroscopy of Trans-Azobenzene: Isomerization Mechanism Following S_2 ($\pi\pi^*$) ← S_0 Photoexcitation

FUJINO, Tatsuya; ARZHANTSEV, Sergei, Yu.; TAHARA, Tahei[1]
([1]IMS and RIKEN)

[*Bull. Chem. Soc. Jpn.* **75**, 1031 (2002)]

Photoisomerization dynamics and the electronic relaxation process of *trans*-azobenzene after the $S_2(\pi\pi^*) \leftarrow S_0$ photoexcitation were investigated in solution by femtosecond and picosecond time-resolved spectroscopy (UV-visible absorption, Raman, and fluorescence). Femtosecond time-resolved absorption spectroscopy was performed to observe the transient absorption of the S_2 and S_1 states. Immediately after photoexcitation, a very broad transient absorption peaked at 475 and 600 nm was observed. This transient absorption decayed rapidly within 0.5 ps, and this ultrafast component was attributed to the $S_n \leftarrow S_2(\pi\pi^*)$ absorption. After the decay of the S_2 state, a transient absorption showing peaks at 410 nm and 500 nm was observed, which was ascribable to the S_1 state. This transient absorption is similar to the $S_n \leftarrow S_1$ absorption that is observed after $S_1 \leftarrow S_0$ photoexcitation. Picosecond time-resolved Raman measurements were carried out to obtain information about the molecular structure of azobenzene in the S_1 state. The NN stretching frequency in the S_1 spectrum was determined with use of ^{15}N-substituted azobenzene, and it was found that the NN stretching frequency in the S_1 state is very close to that in the S_0 state (1428 cm^{-1} in the S_1 and 1440 cm^{-1} in the S_0). This fact indicated that the NN bond retains a double bond character in the S_1 state. A good similarity was also found between the S_1 and S_0 Raman spectrum. The double bond nature of the NN bond as well as a good similarity between the S_1 and S_0 Raman spectra indicates that the observed S_1 state has a planar structure around the NN bond. The Raman data indicate that the observed S_1 state is not a twisted excited state that appears during the rotational isomerization, but the excited state that is populated during the $S_2 \rightarrow S_1 \rightarrow S_0$ relaxation process retaining a planar molecular structure. Anti-Stokes Raman measurements were performed to obtain information about the vibrational relaxation process. The anti-Stokes Raman spectra showed that the S_1 state was highly vibrationally excited. It was also observed that the hot bands due to the S_0 state appear after the decay of the S_1 state and that the S_0 hot bands disappear with a time constant of ~ 16 ps in hexane. Femtosecond time-resolved and steady-state fluorescence spectroscopy was performed and it revealed that the $S_2 \rightarrow$ 'planar' S_1 relaxation process is the major relaxation pathway following S_2 photoexcitation. The quantum yield of the $S_2 \rightarrow$ 'planar' S_1 electric relaxation was evaluated by comparing the intensity of the S_2 and S_1 fluorescence, and it was found to be almost unity. A series of time-resolved spectroscopy demonstrated that the S_2 rotational isomerization pathway, which had been believed so far, does not exist. It has been clarified that the isomerization occurs in the S_1 state after $S_2 \rightarrow S_1$ relaxation. Consequently, it is concluded that the isomerization of azobenzene takes place in the S_1 state by inversion in both cases of S_2 and S_1 photoexcitation.

VI-D-2 Ultrafast Fluorescence of the Chromophore of the Green Fluorescent Protein in Alcohol Solutions

MANDAL, Debabrata; TAHARA, Tahei[1]; WEBBER, N. M.[2]; MEECH, S. R.[2]
([1]IMS and RIKEN; [2]Univ. East Anglia)

[*Chem. Phys. Lett.* **358**, 495 (2002)]

The ultrafast fluorescence dynamics of solutions of the chromophore responsible for emission from the Green Fluorescent Protein are measured by fluorescence up-conversion. Decays are non-exponential but well fit by a sum of two-exponentials. All decays have a prompt rise time. The two decay times are approximately independent of wavelength, but their weights are wavelength dependent, in a manner consistent with a spectral narrowing with time. The longer decay time has a weak dependence on medium viscosity.

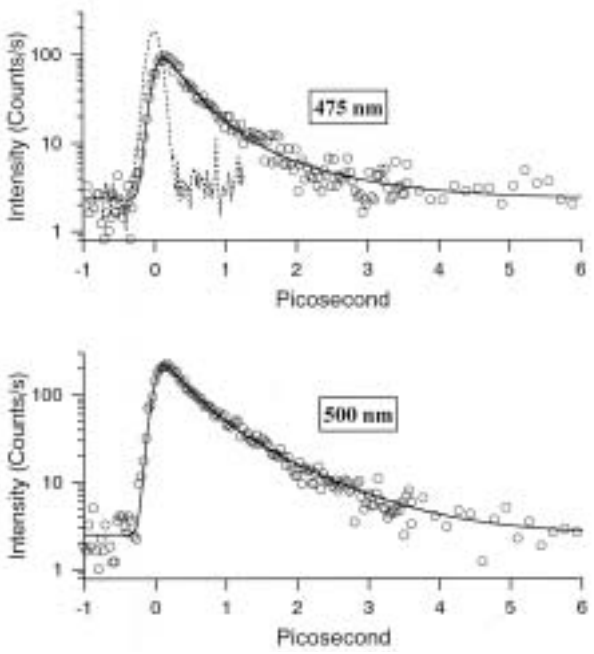

Figure 1. Fluorescence decay data for the anion of **I** in basic methanol, measured as a function of the emission wavelength. The data are fit to a sum of two exponential terms (solid line). Also shown in the 475 nm data is the instrument response function to illustrate time resolution.

VI-D-3 Femtosecond Study of Solvation Dynamics of DCM in Micelles

MANDAL, Debabrata; SOBHAN, Sen[1]; TAHARA, Tahei[2]; BHATTACHARYYA, Kankan[1]
([1]Indian Association Cultivation Sci.; [2]IMS and RIKEN)

[*Chem. Phys. Lett.* **359**, 77 (2002)]

Solvation dynamics of 4-(dicyanomethylene)-2-methyl-6-(p-dimethylamino-styryl) 4H-pyran (DCM) has been studied in neutral (triton X-100, TX) and cationic (cetyl trimethyl ammonium bromide, CTAB) micelles using femtosecond upconversion. Since DCM is insoluble in bulk water the observed solvation dynamics reports the relaxation dynamics exclusively at the micellar interface. It is observed that the solvation dynamics in TX is slower than that in CTAB. The solvation dynamics is described by components of 2.1, 165 and 2050 ps for TX and 0.23, 6.5 (average 1.75 ps) and 350 ps for CTAB.

VI-E Studies of Photochemical Reactions Using Picosecond Time-Resolved Vibrational Spectroscopy

Time-resolved vibrational spectroscopy is a very powerful tool for the study of short-lived transient species. It often affords detailed information about the molecular structure of transients, which is not obtainable with time-resolved electronic spectroscopy. However, for molecules in the condensed phase, we need energy resolution as high as 10 cm^{-1} in order to obtain well-resolved vibrational spectra. This energy resolution is compatible only with time-resolution slower than one picosecond because of the limitation of the uncertainty principle. In this sense, picosecond measurements are the best compromise between energy resolution and time resolution for time-resolved frequency-domain vibrational spectroscopy. In this project, we study photochemical processes and/or short-lived transient species by using picosecond time-resolved Raman spectroscopy.

VI-E-1 Picosecond Time-Resolved Raman Study of the Solvated Electron in Water

MIZUNO, Misao; TAHARA, Tahei[1]
([1]IMS and RIKEN)

[*J. Phys. Chem. A* submitted]

Picosecond time-resolved Raman spectra of water were measured under the resonance condition with the electronic transition of the solvated electron. Transient Raman bands were observed in the OH bend and OH stretch regions in accordance with the generation of the solvated electron. The lifetime of the transient Raman bands were shortened by the addition of the electron scavenger, in exactly the same manner as the solvated electron absorption. It was concluded that the observed transient Raman bands are attributed to the water molecules that directly interact with the electron in the first solvation shell. The resonance enhancement factors were estimated as high as ~ 10^5 (the OH bend) and ~ 10^3 (the OH stretch) when the probe wavelength was tuned to the absorption maximum of the $s \rightarrow p$ transition of the solvated electron. This very high resonance enhancement indicated that the vibrational state of the solvating water molecules are strongly coupled with the electronic state of the electron, and that it is necessary to consider them together when we consider the vibronic state of the local solvation structure. The probe wavelength dependence of the transient Raman intensity was examined in a wide range from 410 nm to 800 nm. The obtained excitation profiles suggested that the $s \rightarrow$ conduction transition does not significantly contribute the resonance Raman enhancement. The polarized Raman measurement was also undertaken for the OH bend band. The non-zero depolarization ratio was observed, which implied that the nondegeneracy of the three sublevels in the excited p state can be observed in a time scale of the Raman process. The OH bending and OH stretching frequencies of the solvating water molecule are red-shifted compared with the frequencies of the bulk water, indicating a structural change is induced by the strong interaction with the electron.

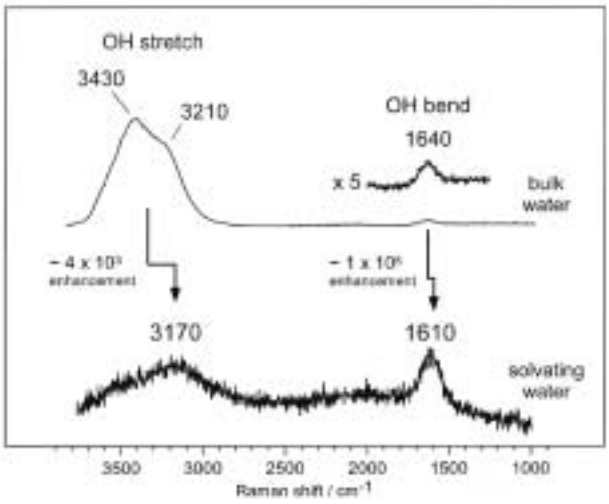

Figure 1. The non-resonance Raman spectrum of bulk water (top; 600 nm excitation) and the resonance Raman spectrum of the water molecules that solvate the electron (bottom; 620 nm excitation).

VI-E-2 Observation of Resonance Hyper-Raman Scattering from all-trans-Retinal

MIZUNO, Misao; HAMAGUCHI, Hiro-o[1]; TAHARA, Tahei[2]
([1]Univ. Tokyo; [2]IMS and RIKEN)

[*J. Phys. Chem. A* **106**, 3599 (2002)]

Hyper-Raman scattering of *all-trans*-retinal was measured for the first time in solution at room tempera-

ture. Under the two-photon resonance condition, the intensity of hyper-Raman scattering was so strong that it could be measured from a diluted solution at concentration as low as 1×10^{-3} mol dm^{-3}. Hyper-Raman excitation profiles were examined in the excitation wavelength range from 770 nm to 840 nm ($\lambda_{ex}/2$: 385–420 nm). In this excitation range, the intensity of all the hyper-Raman bands monotonously increased with shortening excitation wavelength, and the hyper-Raman spectral feature was very similar to that of resonance Raman spectra excited with double the excitation energy ($\lambda_{ex}/2$). The resonance mechanism of hyper-Raman scattering was discussed and it was concluded that hyper-Raman scattering gains intensity enhancement from a two-photon resonance with the "^1B_u*" state, not with the "^1A_g*" state, through the Frank-Condon (the *A* term) mechanism.

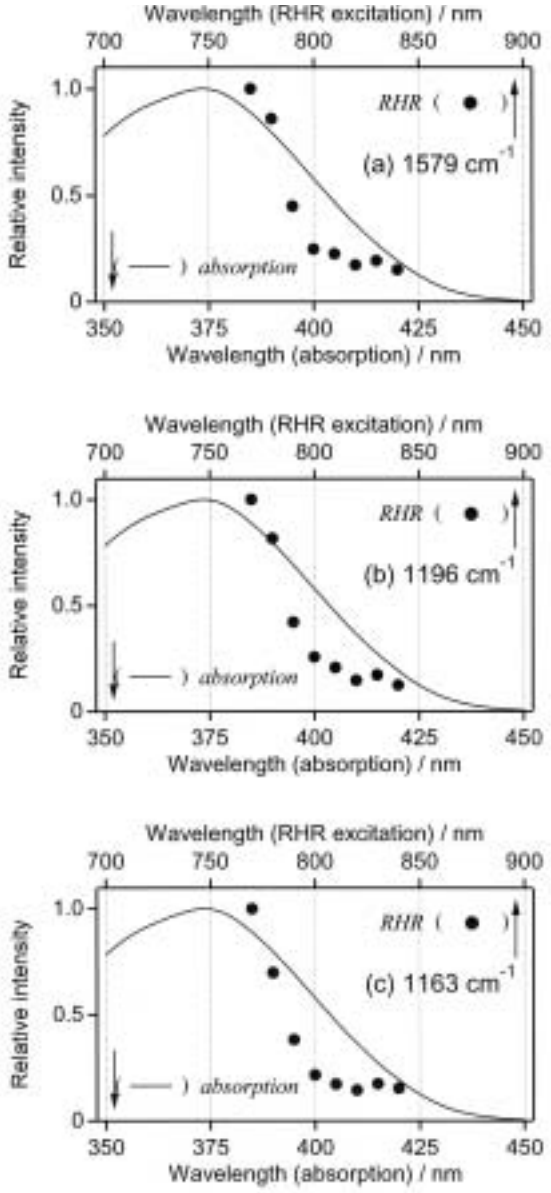

Figure 1. The hyper-Raman excitation profiles of (a) 1579 cm^{-1} (the C=C stretch), (b) 1196 cm^{-1} (the C–C stretch), and (c) 1163 cm^{-1} (the C–C stretch). Black circles and solid lines indicate the intensity of resonance hyper-Raman (RHR) bands and one-photon absorption spectrum, respectively. The excitation profiles of each hyper-Raman band have been normalized by the hyper-Raman intensity measured at 770 nm.

VI-F Synchrotron Radiation Stimulated Surface Reaction and Nanoscience

Synchrotron radiation (SR) stimulated process (etching, CVD) has excellent characteristics of unique material selectivity, low damage, low contamination, high spatial resolution, and high precision *etc*. In this project, nanolevel controlled structures are created by using synchrotron radiation stimulated process, and the reaction mechanisms are investigated by using STM and AFM. Concerning the SR etching, we are considering to apply this technique to the microfabrication of integrated protein transistor circuits.

VI-F-1 Patterning SiO_2 Thin Films Using Synchrotron Radiation Stimulated Etching with a Co Contact Mask

WANG, Changshun[1]; WANG, Zhihong; MORÉ, Sam D. ; YAMAMURA, Shusaku; NONOGAKI, Youichi; URISU, Tsuneo
([1]Henan Univ.)

[*J. Vac. Sci. Technol., B* submitted]

Patterning SiO_2 thin films on Si(100) surface was successfully demonstrated using the synchrotron radiation (SR) stimulated etching with the $SF_6 + O_2$ as the reaction gas and a Co contact mask, as shown in Figure 1. The etching completely stopped at the SiO_2/Si(100) interface. The morphology of the Si surface after the etching, evaluated by the atomic force microscopy (AFM), was almost atomically flat ($R_a \sim 0.33$ nm), and an well-ordered self-assembled monolayer (SAM) of dodecene was deposited on the SR etched region area-selectively, as shown in Figure 2. Co was found to show sufficient resistivity against the SR etching as a mask material and to be easily removed by a dilute acid, without damaging the SAM. The SR etching of the SiO_2 thin films on the Si surface with the Co contact mask is a suitable patterning technique for the area-selective deposition of alkyl SAMs.

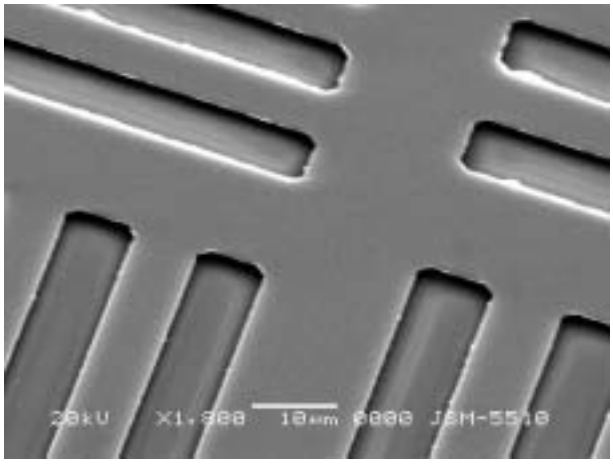

Figure 1. The SEM image of the pattern obtained by the SR etching SiO_2.

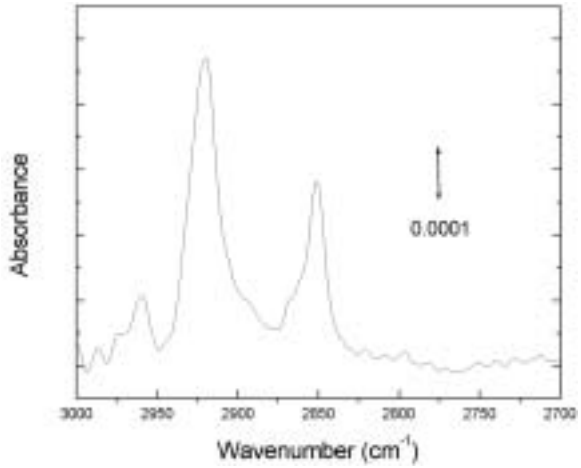

Figure 2. An IRTS of the dodecene SAM deposited on the SR etched surface.

VI-G Noble Semiconductor Surface Vibration Spectroscopy

As a new high sensitive and high resolution surface vibration spectroscopy technique, we are developing an infrared reflection absorption spectroscopy using buried metal layer substrate (BML-IRRAS), which have unique characteristics of high resolution and high sensitivity at finger print regions. Several Si surface chemical reactions are investigated using this BML-IRRAS. As a new fabrication technique of BML substrate, we have almost succeeded in developing the wafer bonding technique. It is considered that BML-IRRAS is also extremely useful in the research of bio-material integration on Si substrates.

VI-G-1 Infrared Reflection Absorption Spectroscopy Using $CoSi_2$ Buried Metal Layer Substrate Made by Wafer-Bonding

YAMAMURA, Shusaku; YAMAUCHI, Shouichi[1]; WATANABE, Satoru[2]; TABE, Michiharu[3]; KASAI, Toshio[4]; NONOGAKI, Youichi; URISU, Tsuneo
([1]DENSO Res. Lab.; [2]Fujitsu Lab.; [3]Shizuoka Univ. ; [4]Saitama Univ.)

[*Jpn. J. Appl. Phys.* submitted]

The conventional infrared reflection absorption spectroscopy (IRRAS) covers wide energy regions including so-called finger print region with sub-monolayer sensitivity. However, it is applicable only for the metal. Therefore we have developed the IRRAS using buried metal layer (BML) substrate. BML wafers have been made so far by ion implantation method. This methods, however, has several problems. A large ion current required for the ion implantation often cause the breakdown of the ion implanter. It is difficult to remove the surface roughness due to the ion implantation damage even after epitaxial growth. Wafer-bonding technique have a possibility to solve these. We have fabricated BML substrates with atom-level flat surfaces by a wafer-bonding technique with a Co deposited Si (100) wafer and SIMOX or SOI wafer (Figure 1). Using the BML substrate fabricated by this method, we successfully observed the stretching and bending vibration bands of self-assembled alkyl monolayers of octadecyltrichlorosilane (OTS) and octenyltrichlorosilane (OTTS) on the Si (100) surface.

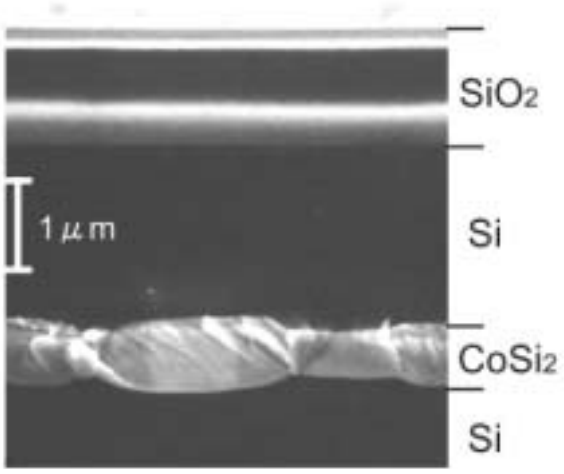

Figure 1. Cross-sectional SEM image of Si(100)/$CoSi_2$/Si(100) BML substrate made from the SOI wafer.

VI-G-2 Hydrogen Diffusion and Chemical Reactivity with Water on Nearly Ideally H-Terminated Si(100) Surface

WANG, Zhihong; NODA, Hideyuki[1]; NONOGAKI, Youichi; YABUMOTO, Norikuni[2]; URISU, Tsuneo
([1]Hitachi Ltd.,; [2]NTT Adv. Tech. Corp.)

[*Jpn. J. Appl. Phys.* **41**, 4275 (2002)]

A nearly ideally H-terminated condition for a Si(100) 2×1 surface is determined from the dependence of the peak intensity and the linewidth of the coupled monohydride symmetric stretching vibration on the hydrogen exposure and exposure temperature, which has been investigated with infrared reflection absorption spectroscopy (IRRAS) using $CoSi_2$ buried metal layer substrate. Even for nearly ideally H-terminated surfaces, the linewidth significantly changes depending on the hydrogen exposure and the exposure temperature. The concentration of deuterium atoms incorporated in the Si bulk is measured by temperature programmed desorption, and it is concluded that hydrogen diffusion into the subsurface of Si has a significant influence on the linewidth broadening. The chemical reactivity with water on the H-terminated Si surface is also investigated.

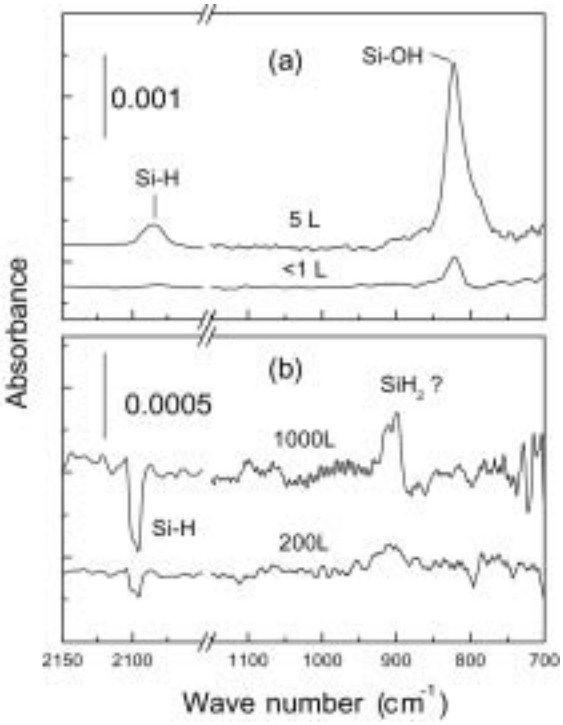

Figure 1. Observed BML-IRRAS spectra (circles) of atomic H-exposed H_2O: Si(100)-(2×1) surfaces at T_m = 373 K for D = 1000 L (top) and D = 50 L (bottom). The results of curve-resolutions assuming a Lorenzian form are compared (solid and dotted lines).

VI-G-3 Atomic Hydrogen-Induced Oxidation on Water-Adsorbed Si(100)-(2×1) Surfaces

WANG, Zhihong; URISU, Tsuneo; NANBU, Shinkoh; MAKI, Jun; AOYAGI, Mutsumi; WATANABE, Hidekazu[1]; OOI, Kenta[1]
([1]Natl. Inst. Adv. Ind. Sci. Tech.)

[*Phys. Rev. B* submitted]

Infrared reflection absorption spectroscopy using buried metal layer substrates (BML-IRRAS) and density functional cluster calculations are used to analyze the atomic hydrogen-induced oxidation on water-adsorbed Si(100)-(2x1) surfaces. In addition to the oxygen inserted coupled monohydrides previously reported, zero, one and two oxygen inserted dihydride species have been

clearly observed for the first time due to the high sensitivity of BML-IRRAS for the perpendicular dynamic dipole moment in the finger print region. It is also found that double oxygen insertion is clearly favored over single oxygen insertions. A new oxidation mechanism, H–Si–Si–OH + 2H → SiH_2 + $Si(O)H_2$ is proposed. In high exposure regions, H–Si–O–Si–H + 2H → SiH_2 + $Si(O)H_2$ reaction is also observed.

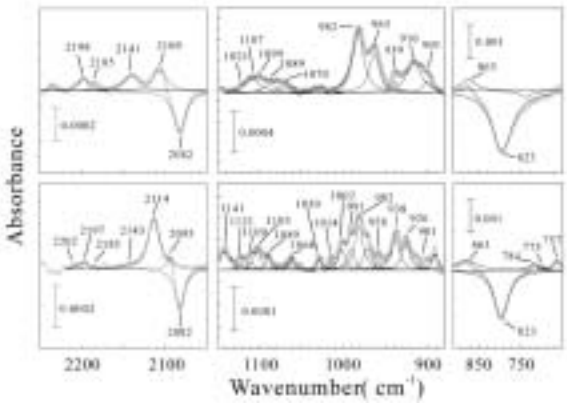

Figure 1. Change of the BML-IRRAS spectra by exposing to water at 373 K, (a) in the case of clean Si(100)(2×1) surface, and (b) nearly ideally H-terminated Si(100)(2×1) surface.

VI-H Integration of Bio-Functional Materials on Silicon

Integration of bio-functional materials such as lipids and proteins are expected to find important applications in biosensors, development of new medicines, and diagnosis of intractable diseases *etc*. In this project, we are investigating the area selective modification of Si surfaces by depositing the self assembled alkyl monolayers, and the integration of lipid bilayers supporting channel proteins keeping their bio-activities. Our special interests are developing "protein transistors" and co-integrating them together with the Si MOS FETs on the same Si chip.

VI-H-1 Hydrophobic/Hydrophilic Interactions of Cytochrome *c* with Functionalized Self-Assembled Monolayers on Silicon

MORÉ, Sam D. ; HUDECECK, Jiri[1]; URISU, Tsuneo
([1]Charles Univ.)

[*Surf. Sci.* in press]

Cytochrome *c* (horse heart) has been adsorbed onto self-assembled monolayers (SAM) on silicon single crystal substrates. Layer thickness was determined using ellipsometry and atomic force microscopy (AFM) in the DFM tapping mode in air. Both hydrophilic (COOH containing SAM) and hydrophobic self-assembled monolayers were used. The protein layers were found to consist of adsorbed 2-dimensional islands.

Concentration, exposure time and the defect-density of the self-assembled monolayer substrates determined the wetting properties of the resulting layer, indicating that the surface orientation of the protein is driven by the interaction with the substrate. On well ordered self-assembled monolayers, the protein layer thicknesses were 1.76 nm for charged surfaces and 2.3 nm for hydrophobic surfaces. Self-assembled monolayers of a lower density resulted in a prevalence of cytochrome *c* islands of 3.2 nm thickness for both cases.

Defects in the SAM facilitate protein adsorption, a denser monolayer of a third orientation type, which leads to the largest adsorbed protein density. At the protein-film air interface 2-dimensional protein islands form, which can be manipulated with an AFM tip in the case of CH_3-terminated SAMs, but not in the case of COO– containing layers.

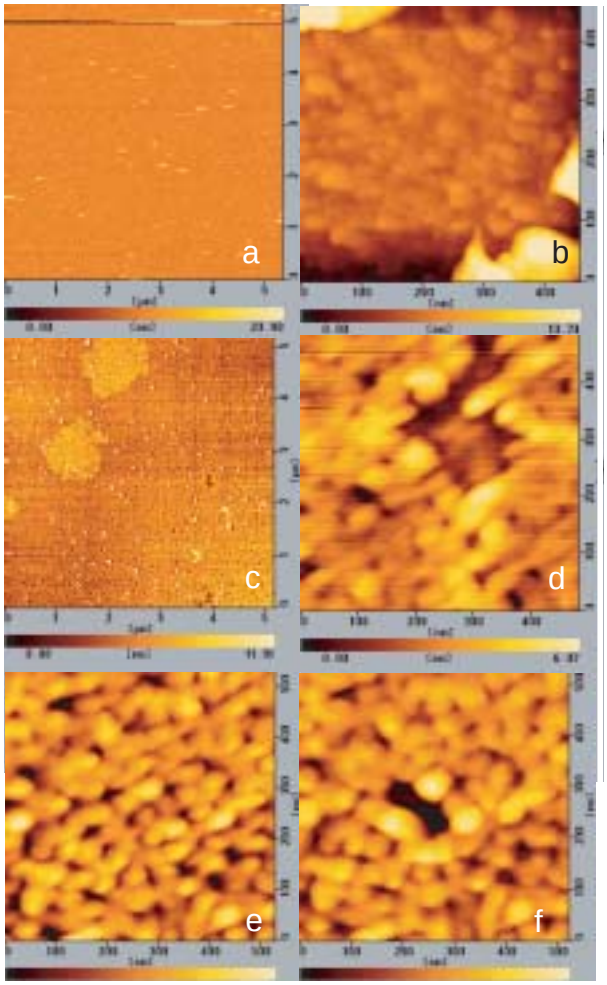

Figure 1. (a) and (b) eicocene terminated SAM prior protein adsorption, (c) and (d) after protein adsorption on a SAM with large defect density. (e) and (f) after selective movement of protein islands into the second layer.

VI-H-2 Influence of Substrate Roughness on the Formation of Self-Assembled Monolayers (SAM) on Silicon(100)

MORÉ, Sam D. ; GRAAF, Harald; BAUNE, Micheal[1]; WANG, Changshun; URISU, Tsuneo
([1]Bremen Univ.)

[*Jpn. J. Appl. Phys.* **41**, 4390 (2002)]

The peak shifts of the CH_2-vibration are an indicator of the amount of gauche-conformational disorder present in aliphatic self-assembled monolayers (SAM). The property of the SAM layer was characterized by measuring the $-CH_3$ and $-CH_2$ stretching vibration modes using FTIR transmission spectroscopy, investigating the relationship between the surface roughness and the peak position as a function of temperature and alkyl chain-length. With increasing substrate surface roughness both the symmetric CH_2-peak as well as the asymmetric CH_2-peak shift to higher wave numbers. The magnitude of the shift is about 6 cm^{-1} at 150 °C and is due to a change from a condensed, almost *all-trans* conformational phase to liquid like layers.

For polished substrates although increased temperatures lead to a slightly more ordered SAM, the layers were in almost an "*all-trans*"-conformational phase independent on the coverage. From these results an "island growth and annealing effect"-model is proposed, which explains relation between the disorder increase and the surface roughness.

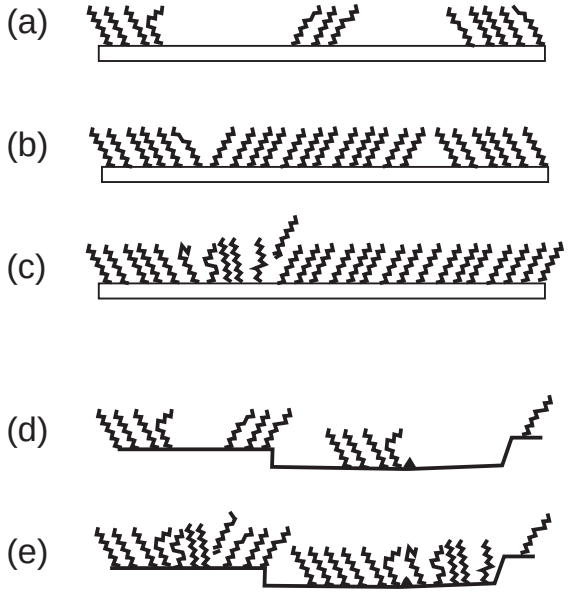

Figure 1. Model for SAM layer growth on flat and rough surfaces explaining the increase of disorder on rough surfaces. (a) Self assembled monolayer starts to form at several sites on the flat Si-surface (b) Domain formation due to different nucleation sites. Monolayer orders itsself due to van der Waals forces (c) Domains anneal and gaps are filled with additional molecules, if the temperature is high enough and the reaction time is sufficient. (d) Self-assembled monolayer starts to form at many sites on the rough surface (e) Self-assembled monolayer starts to anneal, but steps and defects inhibit the annealing process, as the overlap between the chains at the steps is too small. The relative but not the absolute surface coverage is smaller and the disorder, due to gauche defects, larger.

VI-I Photoionization and Photodissociation Dynamics Studied by Electron and Fluorescence Spectroscopy

Molecular photoionization is a major phenomenon in vacuum UV excitation and provides a large amount of information on fundamental electron-core interactions in molecules. Especially, neutral resonance states become of main interest, since they often dominate photoabsorption cross sections and lead to various vibronic states which are inaccessible in direct ionization. We have developed a versatile machine for photoelectron spectroscopy in order to elucidate dynamical aspects of superexcited states such as autoionization, resonance Auger decay, predissociation, vibronic couplings, and internal conversion. Two-dimensional photoelectron spectroscopy, allows us to investigate superexcited states in the valence excitation region of acetylene, nitric oxide, carbonyl sulfide, sulfur dioxide and so on. In this method, the photoelectron yield is measured as a function of both photon energy and electron kinetic energy (binding energy). The spectrum, usually represented as a contour plot, contains rich information on photoionization dynamics.

Photofragmentation into ionic and/or neutral species is also one of the most important phenomena in the vacuum UV excitation. In some cases, the fragments possess sufficient internal energy to de-excite radiatively by emitting UV or visible fluorescence. It is widely accepted that fluorescence spectroscopy is an important tool to determine the fragments and to clarify the mechanisms governing the dissociation processes of diatomic and polyatomic molecules. This year we have carried out fluorescence spectroscopy of H_2O in the photon energy region of 15–30 eV.

VI-I-1 Formation and Autoionization of a Dipole-Forbidden Superexcited State of CS_2

HIKOSAKA, Yasumasa[1]; MITSUKE, Koichiro
([1]Inst. Mater. Struct. Sci.)

[*J. Phys. Chem. A* **105**, 8130 (2001)]

Two-dimensional photoelectron spectroscopy has been performed in the photon energy region of 14.60–15.35 eV, to investigate forbidden superexcited states of CS_2. The two-dimensional photoelectron spectra for the $CS_2^+(\tilde{X}\,^2\Pi_g)$ and $CS_2^+(\tilde{B}\,^2\Sigma_u^+)$ bands show remarkable formation of vibrational levels excited with one quantum of the antisymmetric stretch vibrational mode at $E_{h\nu} \sim 14.88$ eV. This vibrational excitation is attributable to autoionization from a dipole-forbidden superexcited state which is formed through vibronic interaction with the $5p\sigma_u$ Rydberg state converging to $CS_2^+(\tilde{C}^2\Sigma_g^+)$. The forbidden superexcited state is assigned as the $v = 1$ vibrational state in the ν_3 mode of the $3d\sigma_g$ Rydberg member converging to $CS_2^+(\tilde{C}\,^2\Sigma_g^+)$. Preference in the autoionization of the forbidden superexcited state was discussed.

VI-I-2 Autoionization and Neutral Dissociation of Superexcited HI Studied by Two-Dimensional Photoelectron Spectroscopy

HIKOSAKA, Yasumasa[1]; MITSUKE, Koichiro
([1]Inst. Mater. Struct. Sci.)

Two-dimensional photoelectron spectroscopy of hydrogen iodide has been performed in the photon energy region of 11.10–14.85 eV, in order to investigate dynamical properties on autoionization and neutral dissociation of Rydberg states HI*(R_A) converging to $HI^+(\tilde{A}\,^2\Sigma^+_{1/2})$. A two-dimensional photoelectron spectrum in Figure 1 exhibits strong vibrational excitation of $HI^+(\tilde{X}\,^2\Pi_{3/2})$ over a photon energy region from ~ 12 to 13.7 eV, which is attributable to autoionizing feature of the $5d\pi$ HI*(R_A) state. Noticeable features around the photon energy region of 13.5–14.5 eV are assigned as resulting from autoionizing transitions from I*[converging to $I^+(^3P_{0\text{ or }1})$] into $I^+(^3P_2)$. The formation mechanism of I* is due to the predissociation of HI*(R_A) by the repulsive HI* state of Rydberg type converging to $HI^+(^4\Pi_{1/2})$.

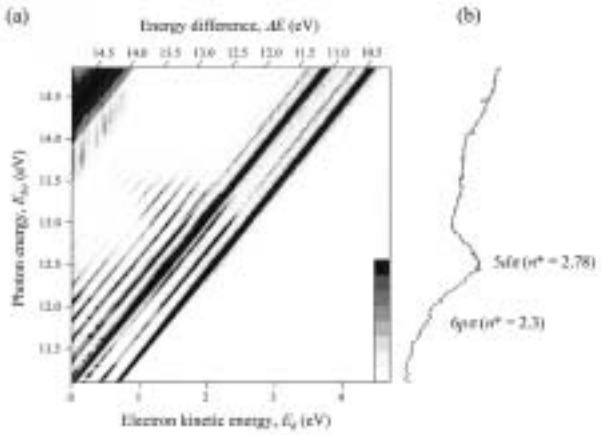

Figure 1. (a) Two-dimensional photoelectron spectrum of HI in the photon energy range of 11.10–14.85 eV. The electron yield, measured as a function of both photon energy $E_{h\nu}$ and electron kinetic energy E_k, is presented by the plots with eight tones from light to dark on a linear scale. The intense structures are truncated. Diagonal lines attached on the top of this figure denote the energy difference defined by $\Delta E = E_{h\nu} - E_k$. (b) The curve obtained by summing electron counts over the whole range of E_k as a function of $E_{h\nu}$.

VI-I-3 Development of the Apparatus for High-Resolution Dispersed Spectroscopy and Fluorescence Excitation Spectroscopy at BL3A2

MITSUKE, Koichiro

The fluorescence was collected by an optical detec-

tion device in Figure 1 made up of spheroidal and spherical mirrors facing each other across the photoexcitation region (*PR*), *i.e.* the source of the fluorescence.[1)] One focal point of the spheroidal mirror fell at *PR*, while the other focal point was at the surface of an optical-fiber bundle. The fluorescence light was reflected back to *PR* by the spherical mirror and was then focused onto the surface of the fiber bundle by the spheroidal mirror. This detection system can collect light from about 62% of the full-sphere solid angle. The fluorescence passed through the optical-fiber bundle (transmission ~ 55% at 400 nm).

In dispersed fluorescence spectroscopy we utilized a 300 mm focal-length imaging spectrograph equipped with a liquid-nitrogen cooled CCD array detector. The overall detection efficiency, including the two mirrors, fiber bundle, and imaging spectrograph, was estimated to be $(1–5) \times 10^{-3}$ with the slit width of the spectrograph being 250 μm. When we fulfilled fluorescence excitation spectroscopy by scanning the wavelength of synchrotron radiation, we replaced the CCD array detector by a photomultiplier tube. In this case, the overall detection efficiency was estimated to be $(1.4 \pm 0.3) \times 10^{-3}$ at the slit widths of the monochromator of 2 mm. All spectra were corrected by the wavelength dependence of the relative detection efficiency.

Reference

1) K. Mitsuke and M. Mizutani, *Bull. Chem. Soc. Jpn.* **74**, 1193 (2001).

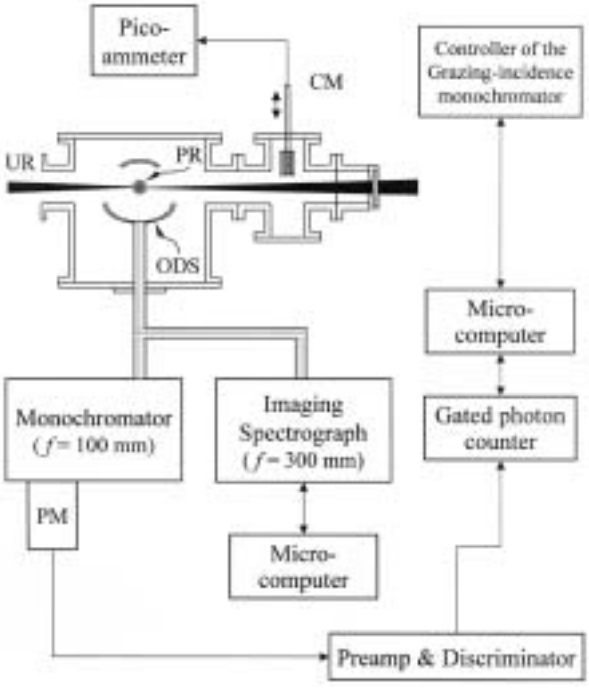

Figure 1. Schematic diagram of the apparatus for dispersed fluorescence spectroscopy and fluorescence excitation spectroscopy. UR, monochromatized undulator radiation; PR, photoexcitation region (not to scale); ODS, optical detection system composed of two mirrors and an optical-fiber bundle; CM, gold-mesh current monitor; PM, photomultiplier.

VI-I-4 UV and Visible Dispersed Spectroscopy for the Photofragments Produced from H_2O in the Extreme Ultraviolet

MITSUKE, Koichiro

[*J. Chem. Phys.* **117**, 8334 (2002)]

The photofragmentation of H_2O has been studied by fluorescence spectroscopy in the photon energy region between $E_{h\nu}$ = 16.9–54.5 eV at the beam line 3A2 of UVSOR. The fluorescence in the wavelength range of 280–720 nm was dispersed with an imaging spectrograph. The dispersed spectra in Figure 1 exhibit the hydrogen Balmer lines of $H^*[n^2L'_{J'} \rightarrow 2^2L''_{J''}$ (n = 3–9) and the emission band systems of H_2O^+ [$\tilde{A}\,^2A_1(0,v'_2,0) \rightarrow \tilde{X}\,^2B_1(0,0,0)$], [$OH^+(\tilde{A}\,\Pi_\Omega, v' \rightarrow \tilde{X}\,^3\Sigma^-, v''$), and $OH(\tilde{A}\,^2\Sigma^+, v' \rightarrow \tilde{X}\,^2\Pi_\Omega, v'')$. The fluorescence cross sections for these transitions have characteristic dependences on $E_{h\nu}$ and vibrational quantum numbers. The cross section summed over the Balmer lines takes a minimum value at $E_{h\nu}$ = 21.7 eV and is very small even at 24.9 eV beyond which it steadily increases with increasing $E_{h\nu}$. This behavior is understood as that the superexcited states correlating with $H^*(n \geq 3)$ + $OH(\tilde{A}\,^2\Sigma^+)$ are too repulsive to be accessible below $E_{h\nu}$ ~ 30 eV by the Franck-Condon transitions from $H_2O(\tilde{X}\,^1A_1)$ and as that the Balmer emission below 30 eV is mainly due to the $H^*(n \geq 3)$ + $H(n = 1)$ + $O(^3P_g)$ channel. The appearance energy 25.5 ± 0.3 eV of the $OH^+(\tilde{A}\,^3\Pi_\Omega, v' \rightarrow \tilde{X}\,^3\Sigma^-, v'')$ transitions is much higher than the dissociation limit of 21.5 eV for the OH^+ $(\tilde{A}\,^3\Pi_\Omega)$ + $H(n = 1)$ channel, but is consistent with the vertical ionization energy to $H_2O^+[(1b_1)^{-2}(4a_1)^1\ ^2A_1]$ that has been assumed to correlate with the above dissociation limit. The vibrational distribution of OH^+ $(\tilde{A}\,^3\Pi_\Omega)$ evaluated from the $OH^+(\tilde{A}\,^3\Pi_\Omega, v' \rightarrow \tilde{X}\,^3\Sigma^-, v'')$ band intensities is similar to the prior distribution in the rigid-rotor harmonic-oscillator approximation.

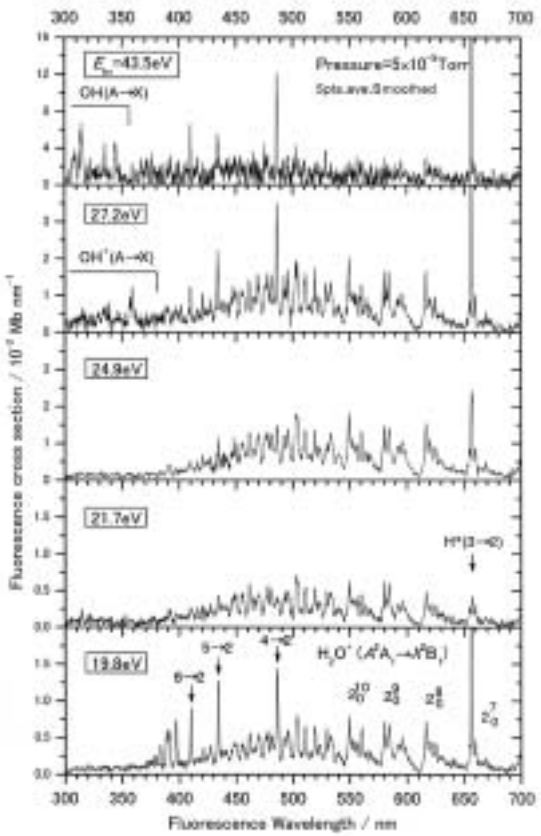

Figure 1. Dispersed fluorescence spectra of H_2O encompassing the wavelength region 300–700 nm at six photon energies between $E_{h\nu}$ = 19.8 and 43.5 eV. The $2_0^{v'_2}$ symbols in the panel of $E_{h\nu}$ = 21.7 eV designate the vibrational progression in the bending mode ν_2 of the $H_2O^+[\tilde{A}\,^2A_1(0,v'_2,0) \rightarrow \tilde{X}\,^2B_1(0,0,0)]$ transition. The hydrogen Balmer lines $H^*[n^2L'_{J'} \rightarrow 2^2L''_{J''}(n$ = 3–9)] are indicated by the ($n \rightarrow 2$) marks.

VI-J Vacuum UV Spectroscopy Making Use of a Combination of Synchrotron Radiation and a Mode-Locked or Pulsed UV Laser

An ultraviolet laser system has been developed which synchronizes precisely with the synchrotron radiation (SR) from the storage ring of the UVSOR facility. A mode-locked Ti:sapphire laser is made to oscillate at the frequency of the ring in a multibunch operation mode. The delay timing between SR and laser pulses can be changed from 0 to 11 ns. The following combination studies have been performed: (1) two-photon ionization of helium atoms studied as the prototype of the time-resolved experiment, (2) laser induced fluorescence (LIF) excitation spectroscopy of $N_2^+(X\ ^2\Sigma_g^+)$ ions produced by synchrotron radiation photoionization of N_2 or N_2O, and (3) LIF excitation spectroscopy of $CN(X\ ^2\Sigma^+)$ radicals produced by synchrotron radiation photodissociation of CH_3CN.

VI-J-1 Partial Photoionization Cross Sections for $N_2^+(X\ ^2\Sigma_g^+, v_X = 0, 1)$ Measured by a Laser Synchrotron Radiation Combination Technique

MITSUKE, Koichiro; MATSUMURA, Hisashi[1]
([1]Chiba Univ.)

[*J. Electron Spectrosc. Relat. Phenom.* submitted]

Molecular superexcited states undergo autoionization into various vibrational levels of a low-lying ionic state with branching ratios *BR* considerably different from those for the direct ionization. The *BR* values are determined chiefly by the molecular constants on the potential energy surfaces involved and transition probabilities for autoionization. In this study, N_2 is subjected to photoionization with the monochromatized undulator radiation into $N_2^+(X\ ^2\Sigma_g^+, v_X = 0$ or 1) which is then probed by LIF excitation spectroscopy in the laser wavelength of the $(B\ ^2\Sigma_u^+, v_B = 0$ or 1) $\leftarrow (X\ ^2\Sigma_g^+, v_X =$ 0 or 1) transition, respectively. Partial cross sections for production of $N_2^+(X\ ^2\Sigma_g^+, v_X = 0$ and 1) are measured as a function of the undulator photon energy. The cross section curves show peaks originating from transitions to Rydberg states converging to $N_2^+(A\ ^2\Pi_u, v_A = 0$–4). Relative peak intensities differ from the $v_X = 0$ to 1 curves. Vibrational *BR*s resulting from autoionization of $N_2^+(A\ ^2\Pi_u)$ were studied by a Franck-Condon Analysis.

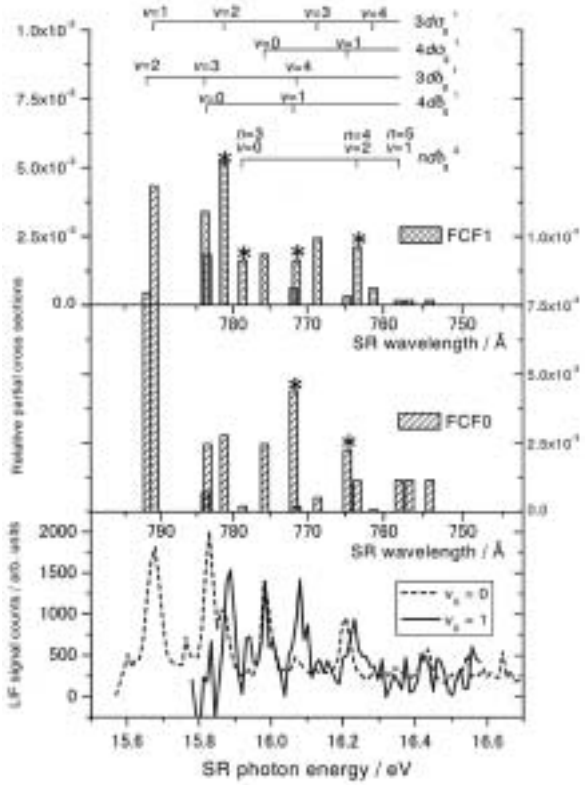

Figure 1. (Lowest Panel) Yield curves of N_2^+ ($X\ ^2\Sigma_g^+$, v_X = 0 or 1) from N_2 obtained from the LIF count rate of the (B, v_B = 0 and 1) → (X, v_X= 1 or 2) transitions, respectively. (Upper two panels) Partial cross sections for production of N_2^+($X\ ^2\Sigma_g^+$, v_X = 0 and 1) calculated by Franck-Condon Analysis.

VI-K Extreme UV Photoionization Studies by Employing a Dragon-Type Grazing-Incidence Monochromator

On the beam line BL2B2 in UVSOR a grazing incidence monochromator has been constructed which supplies photons in the energy region from 20 to 200 eV [M. Ono, H. Yoshida, H. Hattori and K. Mitsuke, *Nucl. Instrum. Methods Phys. Res., Sect. A* **467-468**, 577 (2001)]. This monochromator has bridged the energy gap between the beam lines BL3A2 and BL8B1, thus providing for an accelerating demand for the high-resolution and high-flux photon beam from the research fields of photoexcitation of inner-valence electrons, *L*-shell electrons in the third-row atom, and 4*d* electrons of the lanthanides.

Since 2001 we have tried taking photoion yield curves of fullerenes at BL2B2. Geometrical structures and electronic properties of fullerenes have attracted widespread attention because of their novel structures, novel reactivity, and novel catalytic behaviors as typical nanometer-size materials. Moreover, it has been emphasized that the potential for the development of fullerenes to superconductors (T_c ~ 50 K) and strong ferromagnetic substances is extremely high. In spite of such important species spectroscopic information is very limited in the extreme UV region, which has been probably due to difficulties in obtaining enough amount of sample. The situation has been rapidly changed in these few years, since the techniques of syntheses, isolation, and purification have been advanced so rapidly that appreciable amount of fullerenes is obtainable from several distributors in Japan.

VI-K-1 Anisotropy of Fragment Ions from SF_6 by Photoexcitation of a Valence- or Sulfur 2*p*-Electron between 23 and 210 eV

ONO, Masaki[1]; MITSUKE, Koichiro
([1]Louisiana State Univ.)

[*Chem. Phys. Lett.* in press]

The anisotropy of the fragment ions produced by photoexcitation of SF_6 has been measured using synchrotron radiation in the energy range of 23–210 eV. In spite of the highly symmetrical molecule the strong anisotropy is observed at lower photon energies. Anisotropy gradually decreases with increasing photon energy. The behavior of the curve of the asymmetry parameter has been interpreted qualitatively by means of simulation using partial oscillator strengths for the formation of fragment ions in the region of valence electron excitation (16–63 eV). Only SF_5^+ ions are assumed to have an anisotropic angular distribution, which can be explained in terms of transitions into neutral excited states of valence type. With increasing photon energy the branching ratio for the SF_5^+ ion

decreases, while the contribution of direct photoionization may increase. As a result the asymmetry parameter involving all the fragment ions declines steadily with the photon energy. Moreover, inner valence-electron excitation between 35 and 50 eV is found to open new decay channels which produce photoions isotropically. The asymmetry parameter remains constant at 0.01–0.02 below the sulfur $2p_{3/2,1/2}$ edges (< 180 eV), whether the photon energy is chosen at on- or off-resonance. Above the edges it decreases down to almost zero, in accord with the opening of the *LVV* Auger decay channels.

VI-K-2 Construction of the Photoionization Spectrometer for Fullerenes and Metallofullerenes

MITSUKE, Koichiro; ONO, Masaki[1]; KOU, Junkei; MORI, Takanori; HARUYAMA, Yusuke[2]; KUBOZONO, Yoshihiro
([1]Louisiana State Univ.; [2]Okayama Univ.)

Figure 1 shows the photograph of the apparatus designed to carry out extreme UV photoionization of fullerenes. A copper sample holder is mounted inside a radiation shield made of stainless steel. The vapor of the fullerene discharged from a small orifice is subjected to irradiation of the synchrotron radiation supplied from the Dragon-type monochromator. A drift tube was equipped between parallel plate electrodes placed above the oven unit and the housing of a microchannel plate electron multiplier detector. Insertion of the drift tube allows us to drastically reduce bothering background counts due to stray electrons and impurities and then realize a stable operation of the oven.

In the case of C_{60} the sample of 99.98% purity was purchased and further purified by eliminating organic solvent such as benzene or toluene through heating the sample one day in vacuum at 300 °C. In order to prepare the number density of fullerenes high enough at the interaction volume we increased the temperature of an oven up to 500 °C. The sublimation rate measured by using a quartz-oscillator thickness monitor was around 100–150 ng/s. We were able to find the optimum experimental conditions that keep a steady flow of the C_{60} vapor at the interaction volume.

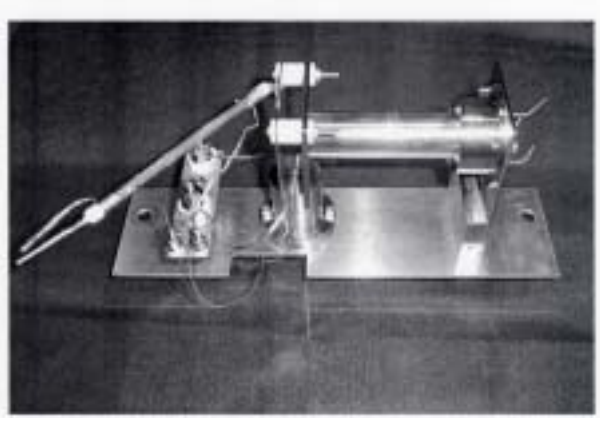

Figure 1. Photograph of the photoionization spectrometer developed for fullerenes.

VI-K-3 Photoion Yield Spectra of C_{60} in the Region of 23–210 eV

MITSUKE, Koichiro; ONO, Masaki[1]; KOU, Junkei; MORI, Takanori; HARUYAMA, Yusuke[2]; KUBOZONO, Yoshihiro
([1]Louisiana State Univ.; [2]Okayama Univ.)

In 1992 Hertel and coworkers have reported the photoionization efficiency curve for C_{60}^+ and revealed an intense broad peak at the photon energy of ~ 20 eV.[1)] They assigned it as resulting from excitation of surface plasmon in C_{60}: Collective longitudinal motion of multiple valence electrons is excited when C_{60} absorbs a transverse-wave light. So far much knowledge has been accumulated in the lower energy side of this plasmon peak, whereas there has been no experimental data between the high energy side and region containing the carbon 1*s* edge (~ 290 eV). This situation motivates us to take the efficiency curve encompassing the range from 23 to 210 eV.

Figure 1 shows a photoion yield curve of C_{60} plotted as a function of the photon energy. Above the three shoulders at 26, 33, and 47 eV the ion yield goes down monotonically with increasing photon energy. Figure 1 also shows representative data points from the literature.[1,2)] Our data depend on the photon energy most weakly and behave similarly to those of Ref. 2) at ≤ 32 eV. The Hertel's spectrum completely differs from the other curves. The three shoulders, appearing only in our spectrum, are attributed to the shape resonance, *i.e.* promotion of an electron up to a vacant valence virtual orbital which is characterized by a high orbital angular momentum.

References

1) I.V. Hertel *et al., Phys. Rev. Lett.* **68**, 784 (1992).
2) Yoo *et al., J. Chem. Phys.* **96**, 911 (1992).

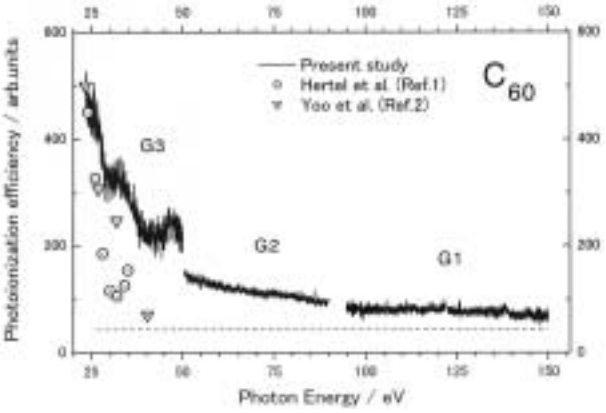

Figure 1. Photoionization efficiency curves of C_{60}.